American Mineralogist, Volume 99, pages 654–666, 2014

Allendeite ($Sc_4Zr_3O_{12}$) and hexamolybdenum (Mo,Ru,Fe), two new minerals from an ultrarefractory inclusion from the Allende meteorite

Chi Ma*, John R. Beckett and George R. Rossman

Division of Geological and Planetary Sciences, California Institute of Technology, Pasadena, California 91125, U.S.A.

Abstract

During a nanomineralogy investigation of the Allende meteorite with analytical scanning electron microscopy, two new minerals were discovered; both occur as micro- to nano-crystals in an ultrarefractory inclusion, *ACM-1*. They are allendeite, $Sc_4Zr_3O_{12}$, a new Sc- and Zr-rich oxide; and hexamolybdenum (Mo,Ru,Fe,Ir,Os), a Mo-dominant alloy. Allendeite is trigonal, $R\bar{3}$, a = 9.396, c = 8.720, V = 666.7 Å^3, and Z = 3, with a calculated density of 4.84 g/cm^3 via the previously described structure and our observed chemistry. Hexamolybdenum is hexagonal, $P6_3/mmc$, a = 2.7506, c = 4.4318 Å, V = 29.04 Å^3, and Z = 2, with a calculated density of 11.90 g/cm^3 via the known structure and our observed chemistry. Allendeite is named after the Allende meteorite. The name hexamolybdenum refers to the symmetry (primitive hexagonal) and composition (Mo-rich). The two minerals reflect conditions during early stages of the formation of the Solar System. Allendeite may have been an important ultrarefractory carrier phase linking Zr-,Sc-oxides to the more common Sc-,Zr-enriched pyroxenes in Ca-Al-rich inclusions. Hexamolybdenum is part of a continuum of high-temperature alloys in meteorites supplying a link between Os- and/or Ru-rich and Fe-rich meteoritic alloys. It may be a derivative of the former and a precursor of the latter.

Keywords: Allendeite, $Sc_4Zr_3O_{12}$, hexamolybdenum, new alloy, new mineral, EBSD, nanomineralogy, Allende meteorite, CV3 carbonaceous chondrite

Introduction

Processes that occurred during the first few million years of our solar system are largely inferred from the study of meteorites and their constituents (e.g., Kerridge and Matthews 1988; Lauretta and McSween 2006). Where the elements and/or isotopes in a mineral are fractionated or one phase is stabilized over another, it is often possible to constrain the nature of the environment and/or the intensity of the process(es) that led to these fractionations and changes in stability. Thus, each new phase adds a new voice and, with appropriate thermodynamic and/or kinetic data, it may also be possible to understand some of the lyrics.

The Allende meteorite, which fell near Pueblito de Allende, Chihuahua, Mexico, on February 8, 1969, is a CV3 carbonaceous chondrite. It is the largest carbonaceous chondrite ever recovered on the Earth and is often called the best-studied meteorite in history. More than four decades after it fell, this meteorite continues to be the source of new discoveries. For example, in the first decade after its fall, Allende yielded at least seven minerals not previously observed in meteorites (Fuchs 1969, 1971; Keil and Fuchs 1971; Fuchs and Blander 1977; Lovering et al. 1979) and, in the last several years, Allende has yielded another 18 minerals new to meteorites, 12 of which are also new to science (Ma 2010, 2013a, 2013b; Ma and Rossman 2008b, 2009a, 2009b, 2009c; Ma and Krot 2013; Ma et al. 2009b, 2012, 2013a, 2013b, 2013c, 2014; this work). Overall, Allende, one of nearly 40 000 known meteorites, is the original source of nearly one in ten of the known minerals in meteorites (cf. Rubin 1997). In this work, we describe two of these new minerals, allendeite and hexamolybdenum, which were discovered in an Allende ultrarefractory inclusion, named *ACM-1*. We describe the properties and chemistry of both phases and explore their origin and evolution. Preliminary results of the work reported in this study are given by Ma et al. (2009a).

Mineral names and type materials

The section containing the holotype allendeite specimen was prepared from a 1 cm diameter fragment of Allende (Caltech Meteorite Collection No. Allende-12A) and deposited in the Smithsonian Institution's National Museum of Natural History under catalog number USNM 7554. The holotype hexamolybdenum specimen described in the text, a 1.2 μm crystal occurring with allendeite in USNM 7554, was the crystal most amenable to detailed characterization, but the grain was lost during the attempted ion probe analysis of an adjacent grain. Additional specimens of hexamolybdenum can, however, be found in the Smithsonian Institution's National Museum of Natural History Allende section USNM 3509HC12 and in section USNM 7590 of NWA 1934, another CV3 chondrite. Some of the refractory alloy grains from acid residues of the Murchison CM2 chondrite described by Harries et al. (2012) are also hexamolybdenum.

The name allendeite refers to the host meteorite, Allende, which has proven to be a treasure trove of new minerals, as noted above, and is the target of many important studies on the origin and evolution of the Solar System. The name hexamolybdenum refers to the symmetry (primitive hexagonal) and composition

* E-mail: chi@gps.caltech.edu

0003-004X/14/0004–654$05.00/DOI: http://dx.doi.org/10.2138/am.2014.4667

(Mo-rich) of this refractory alloy. The two minerals and their names have been approved by the Commission on New Minerals, Nomenclature and Classification of the International Mineralogical Association (IMA 2007-027 and IMA 2007-029).

Occurrence and associated minerals

The Allende CV3 carbonaceous chondrite fell within a strewn field near Pueblito de Allende, Chihuahua, Mexico, on February 8, 1969 (Clarke et al. 1970). The minerals allendeite and hexamolybdenum were both found within one ovoid-shaped ~70 ×120 µm ultrarefractory inclusion in one polished section (USNM 7554) of this meteorite (Fig. 1). We used electron backscatter diffraction (EBSD), discussed below, to determine the orientation of crystals in the section and this shows that allendeite ($Sc_4Zr_3O_{12}$) in the upper portion of Figure 1 (Fig. 2) forms a single 15 × 25 µm crystal with included perovskite, Os-Ir-Mo-W alloys, and Sc-stabilized tazheranite (cubic zirconia). There are also both linked and isolated 1–5 µm irregular grains, coexisting with perovskite, hexamolybdenum (Mo,Ru,Fe,Ir,Os), and other Os-, Ir-, Mo-, Ru-, W-rich alloys elsewhere in the inclusion. *ACM-1* is largely altered to nepheline, sodalite, and an aluminous, low-Ti augite, with surviving allendeite invariably in contact with perovskite. Allendeite-nepheline contacts appear sharp and the allendeite does not appear to be embayed. Perovskite, where in contact with alteration phases, is often rimmed by ilmenite. We also observed one grain of Mg-Al spinel in contact with allendeite, hexamolybdenum, and perovskite, and rare Fe-Mg-Al spinels in the altered regions of the inclusion.

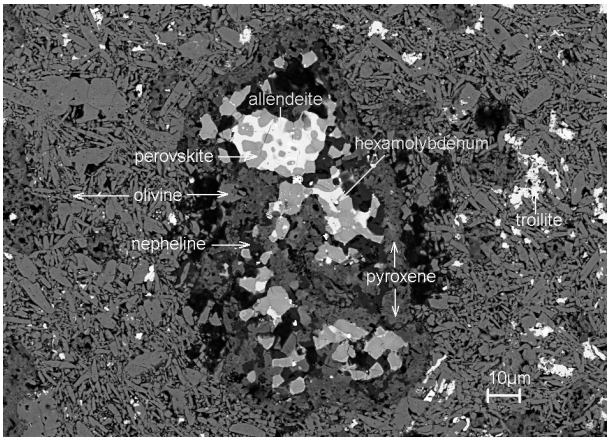

Figure 1. Backscattered electron (BSE) image of the ultrarefractory inclusion *ACM-1* containing allendeite and hexamolybdenum in polished Allende section USNM 7554.

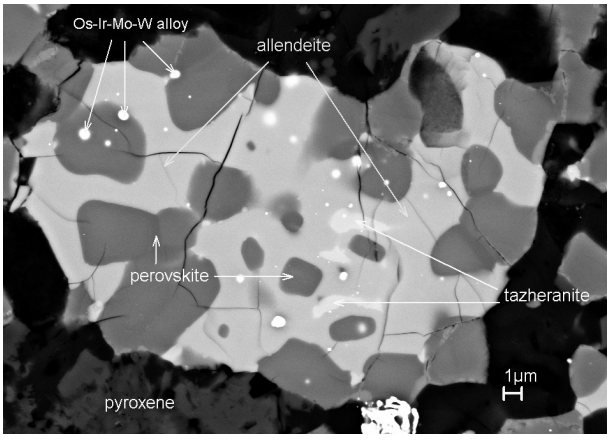

Figure 2. Enlarged BSE image showing a single crystal of allendeite (cf. Fig. 1) with included perovskite, tazheranite, and Os-Ir-Mo-W-rich alloys.

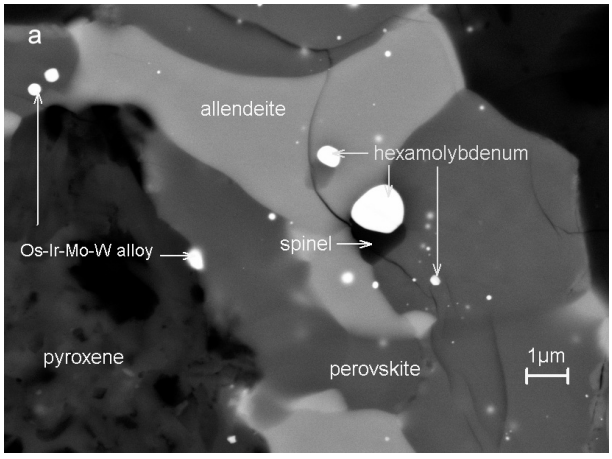

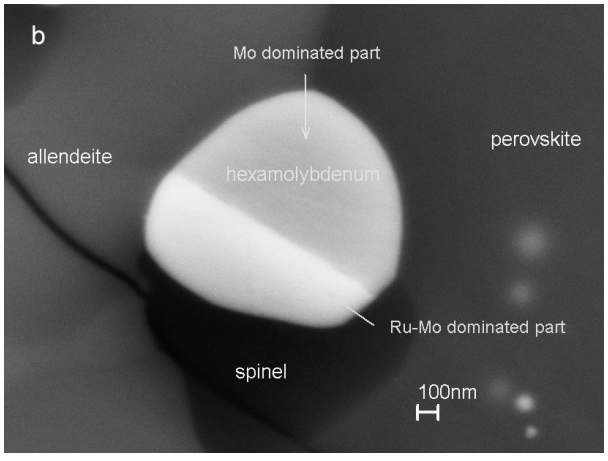

Figure 3. BSE images showing a portion of *ACM-1* (cf. Fig. 1). (**a**) Region containing hexamolybdenum, allendeite, perovskite, and Os-Ir-Mo-W alloys. (**b**) Enlarged BSE image showing the hexamolybdenum crystal (1.2 µm across).

Euhedral hexamolybdenum was initially investigated because it combined strong backscattered electron intensity with clear crystal shapes that contrasted with the anhedral habits of other alloy grains in the same inclusion (Fig. 3). This phase occurs as inclusions in allendeite and a Zr-Y-rich perovskite in USNM 7554. Other Os-Ir-Mo-Ru-W-bearing alloys in which Mo is not the dominant element, tazheranite $(Zr,Sc,Ca,Ti)O_{1.75}$, and spinel are observed within 2 µm (Figs. 1–3; Tables 1–2). Like hexamolybdenum, the more Os-W-Ir enriched alloys in this inclusion have strong backscatter electron intensities but they are invariably anhedral. In USNM 3509HC12, euhedral

hexamolybdenum is included in Ti-Sc-enriched kushiroite and is associated with perovskite.

The 1.2 μm diameter grain of hexamolybdenum in *ACM-1* consists of two compositionally distinct portions. The upper, larger portion of the crystal (Fig. 3b) is a Mo-dominant (hexamolybdenum) phase and the lower brighter (higher Z) part is sufficiently enriched in Ru to be the mineral ruthenium. Analysis by EPMA (Table 2) shows the hexamolybdenum portion of this crystal to have an empirical formula of $Mo_{0.56}Ru_{0.24}Fe_{0.08}Ir_{0.07}Os_{0.03}W_{0.01}Ni_{0.01}$ and the lower, brighter portion $Ru_{0.41}Mo_{0.39}Ir_{0.10}Fe_{0.05}Os_{0.03}W_{0.01}Ni_{0.01}$. EBSD analysis shows that both portions have the same hexagonal structure. The apparently sharp discontinuity in composition suggests either episodic growth or exsolution. The two smaller hexamolybdenum grains shown in Figure 3 are too small for quantitative EPMA but SEM-EDS analysis yielded $Mo_{0.44}Ir_{0.26}Ru_{0.19}Fe_{0.06}W_{0.04}Os_{0.01}$ (larger grain) and $Mo_{0.82}Ru_{0.08}Fe_{0.04}Os_{0.03}W_{0.02}Ir_{0.01}$ (smaller grain). The larger of the two grains was confirmed to be hexamolybdenum by SEM-EDS and EBSD. The simplified formula of hexamolybdenum is: (Mo,Ru,Fe,Ir,Os).

Appearance, physical and optical properties

Allendeite occurs as anhedral grains, as large as 10 × 25 μm in section. Color, streak, luster, hardness, tenacity, cleavage, fracture, density, and refractive index were not determined because of the optically thick section holding the sample and the small grain size. The density, calculated from the empirical formula (Table 1) and the structure as given by Rossell (1976) is 4.84 g/cm^3. Allendeite is not cathodoluminescent under the electron beam of a scanning electron microscope and we observed no crystal forms or twinning.

Hexamolybdenum occurs in *ACM-1* as euhedral, metallic grains, 0.2–1.2 μm in diameter (Figs. 1 and 3). Color, streak, luster, hardness, tenacity, cleavage, fracture, and density could not be determined because of the small grain size. The calculated density is 11.90 g/cm^3 via the structure of Anderson and Hume-Rothery (1960) and our observed chemistry (Table 2). Hexamolybdenum is not cathodoluminescent under the electron beam of an SEM.

Chemical composition

Backscatter electron (BSE) images were obtained with a ZEISS 1550VP field emission SEM and a JEOL 8200 electron microprobe using solid-state BSE detectors. Quantitative elemental microanalyses of allendeite, hexamolybdenum, and associated grains were conducted with the JEOL 8200 electron microprobe operated in a focused beam mode at 15 kV and 10 nA for allendeite and 5 nA for hexamolybdenum. Standards for the analysis of allendeite and associated oxides and silicates were zircon (Zr*L*α), $ScPO_4$ (Sc*K*α), YPO_4 (Y*L*α), Hf metal (Hf*L*α),

Table 1. Oxides and silicates in allendeite- and hexamolybdenum-bearing phase assemblages

Phase	allendeite	perovskite	tazheranite	Mg-Al spinel	Fe-Al spinel	sodalite	nepheline	Al-rich, low-Ti augite	perovskite[a]	pyroxene[a]
Section	USNM 7554	USNM 7554	USNM 7554	USNM 7554	USNM 7554	USNM 7554	USNM 7554	USNM 7554	USNM 3509HC12	USNM 3509HC12
type	EPMA[b]	EPMA	EPMA	SEM-EDS[c]	SEM-EDS	SEM-EDS	SEM-EDS	SEM-EDS	SEM-EDS	SEM-EDS
No. analyses	8	7	2	1	1	1	1	1	1	1
Na_2O	n.d.[d]	n.d.	n.d.	n.d.	n.d.	17.99 (0.46)	12.67 (0.50)	n.d.	n.d.	n.d.
MgO	n.d.	n.d.	n.d.	11.64 (0.20)[c]	12.14 (0.35)	0.91 (0.23)	1.97 (0.33)	4.48 (0.22)	n.d.	2.73 (0.13)
Al_2O_3	0.70 (0.03)[b]	1.26 (0.17)	0.45 (0.04)	33.44 (0.34)	61.28 (0.68)	28.38 (0.64)	29.77 (0.77)	15.80 (0.34)	3.09 (0.17)	27.72 (0.28)
SiO_2	n.d.	n.d.	n.d.	n.d.	1.69 (0.28)	39.24 (0.81)	46.41 (1.07)	42.85(0.53)	n.d.	20.90 (0.28)
Cl	n.d.	n.d.	n.d.	n.d.	n.d.	7.37 (0.29)	n.d.	n.d.	n.d.	n.d.
K_2O	n.d.	n.d.	n.d.	n.d.	n.d.	n.d.	1.63 (0.25)	n.d.	n.d.	n.d.
CaO	2.74 (0.50)	34.26 (1.05)	6.52 (1.07)	17.38 (0.24)	0.63 (0.15)	0.94 (0.24)	2.79 (0.34)	27.67 (0.39)	35.00 (0.39)	22.59 (0.25)
Sc_2O_3	32.36 0.51)	2.50 (1.20)	15.23 1.06)	2.77 (0.20)	n.d.	n.d.	n.d.	n.d.	n.d.	6.72 (0.23)
TiO_2	5.47 (0.89)	48.01 (1.47)	4.84 (1.33)	26.39 (0.37)	n.d.	2.45 (0.43)	n.d.	n.d.	51.70 (0.57)	11.93 (0.28)
V_2O_3	0.35 (0.04)	0.41 (0.08)	0.23 (0.00)	1.16 (0.22)	n.d.	n.d.	n.d.	n.d.	n.d.	1.15 (0.19)
Cr_2O_3	0.02 (0.03)	0.06 (0.03)	0.02 (0.01)	n.d.	n.d.	n.d.	n.d.	n.d.	n.d.	n.d.
FeO*[e]	0.82 (0.04)	0.70 (0.04)	0.87 (0.06)	1.52 (0.22)	24.25 (0.62)	2.73 (0.75)	4.76 (1.04)	9.20 (0.46)	0.87 (0.25)	0.99 (0.19)
Y_2O_3	0.70 (0.07)	3.84 (0.97)	2.12 (0.22)	n.d.	n.d.	n.d.	n.d.	n.d.	7.17 (0.46)	n.d.
ZrO_2	56.58 (1.20)	7.87 (2.29)	68.42 (3.11)	5.70 (0.42)	n.d.	n.d.	n.d.	n.d.	2.17 (0.46)	5.27 (0.34)
HfO_2	1.21 (0.15)	0.14 (0.14)	1.34 (0.10)	n.d.	n.d.	n.d.	n.d.	n.d.	n.d.	n.d.
Total	100.94	99.04	100.04	100.00	100.00	100.01	100.00	100.00	100.00	100.00
No. O atoms	12	3	1.75	4	4	24	4	6	3	6
Na	n.d.	n.d.	n.d.	n.d.	n.d.	5.42	0.58	n.d.	n.d.	n.d.
Mg	n.d.	n.d.	n.d.	0.47	0.48	0.21	0.07	0.25	n.d.	0.16
Al	0.09	0.04	0.01	1.08	1.92	5.20	0.83	0.71	0.08	1.28
Si	n.d.	n.d.	n.d.	n.d.	0.04	6.10	1.10	1.63	n.d.	0.82
Cl	n.d.	n.d.	n.d.	n.d.	n.d.	1.94	n.d.	n.d.	n.d.	n.d.
K	n.d.	n.d.	n.d.	n.d.	n.d.	n.d.	0.05	n.d.	n.d.	n.d.
Ca	0.31	0.87	0.12	0.51	0.02	0.16	0.07	1.13	0.87	0.95
Sc	3.01	0.05	0.22	0.07	n.d.	n.d.	n.d.	n.d.	n.d.	0.23
Ti	0.44	0.86	0.06	0.54	n.d.	0.29	n.d.	n.d.	0.90	0.35
V	0.03	0.01	0.00	0.03	n.d.	n.d.	n.d.	n.d.	n.d.	0.04
Cr	0.00	0.00	0.00	n.d.	n.d.	n.d.	n.d.	n.d.	n.d.	n.d.
Fe*[e]	0.07	0.01	0.01	0.03	0.54	0.36	0.09	0.29	0.02	0.03
Y	0.04	0.05	0.02	n.d.	n.d.	n.d.	n.d.	n.d.	0.09	n.d.
Zr	2.95	0.09	0.55	008	n.d.	n.d.	n.d.	n.d.	0.02	0.10
Hf	0.04	0.00	0.01	n.d.	n.d.	n.d.	n.d.	n.d.	n.d.	n.d.
Sum cations	6.99	4.98	1.00	2.81	3.00	17.74	2.79	4.01	1.99	3.96

[a] Host phases of hexamolybdenum grain in USNM 3509HC12 (analysis given in Table 2).
[b] Errors given inside parentheses are one standard deviation of the mean based on all of the analyses.
[c] Errors given inside parentheses are one standard deviation computed from counting statistics.
[d] n.d.: not determined.
[e] All Fe as FeO.

TABLE 2. Alloys in allendeite- and hexamolybdenum-bearing phase assemblages

Phase	hexamolybdenum grn#1	Ru-dominated region grn#1	hexamolybdenum grn#2	hexamolybdenum grn#3 (smallest)	Os-Ir-Mo-W grn#1	Os-Ir-Mo-W grn#2	Os-Ir-Mo-W grn#3	hexamolybdenum
Section	USNM 7554	USNM 7554	USNM 7554	USNM 7554	USNM 7554	USNM 7554	USNM 7554	USNM 3509HC12
type	EPMA[a]	EPMA	SEM-EDS[b]	SEM-EDS	SEM-EDS	SEM-EDS	SEM-EDS	EPMA
No. analyses	6	2	1	1	1	1	1	8
Fe	4.27 (0.08)[a]	2.47 (0.01)	2.60 (0.30)[b]	1.98 (0.60)	1.71 (0.37)	2.32 (1.37)	2.35 (0.73)	11.84 (0.22)
Ni	0.47 (0.08)	0.29 (0.00)	n.d.	n.d.	n.d.	n.d.	n.d.	1.30 (0.13)
Mo	51.61 (0.46)	29.89 (1.18)	33.62 (0.88)	78.71 (2.29)	6.74 (0.91)	12.12 (1.99)	5.30 (1.21)	20.56 (0.36)
Ru	23.04 (0.63)	33.54 (0.43)	15.78 (0.72)	8.01 (1.45)	1.81 (0.73)	1.56 (1.41)	0.52 (1.03)	19.38 (0.46)
W	1.90 (0.26)	0.96 (0.09)	5.99 (0.57)	2.93 (1.00)	13.19 (0.89)	12.40 (1.59)	12.47 (1.28)	3.10 (0.16)
Re	n.d.[c]	n.d.	n.d.	n.d.	n.d.	n.d.	n.d.	0.96 (0.20)
Os	5.63 (0.66)	4.56 (0.39)	2.01 (1.11)	5.58 (1.48)	51.11 (1.44)	34.66 (2.72)	65.03 (2.18)	17.19 (0.75)
Ir	12.00 (0.81)	15.35 (1.26)	40.01 (0.94)	2.79 (1.34)	25.43 (1.26)	36.94 (2.53)	14.32 (1.82)	15.09 (0.92)
Pt	0.23 (0.38)	0.89 (1.26)	n.d.	n.d.	n.d.	n.d.	n.d.	0.07 (0.13)
Total	99.15	87.95	100.00	100.00	100.00	100.00	100.00	89.51
				at%				
Fe	8.01	5.48	5.78	3.57	5.17	6.64	7.17	25.50
Ni	0.84	0.61	n.d.	n.d.	n.d.	n.d.	n.d.	2.66
Mo	56.39	38.64	43.56	82.46	11.88	20.20	9.41	25.77
Ru	23.90	41.17	19.42	7.96	3.03	2.47	0.88	23.05
W	1.08	0.65	4.05	1.60	12.12	10.79	11.56	2.03
Re	n.d.	n.d.	n.d.	n.d.	n.d.	n.d.	n.d.	0.62
Os	3.10	2.97	1.32	2.95	45.42	29.15	58.28	10.87
Ir	6.55	9.90	25.88	1.46	22.37	30.75	12.70	9.44
Pt	0.12	0.58	n.d.	n.d.	n.d.	n.d.	n.d.	0.04
Sum	100.00	100.00	100.00	100.00	100.00	100.00	100.00	100.00

[a] Errors given inside parentheses are one standard deviation of the mean based on all of the analyses.
[b] Errors given inside parentheses are one standard deviation computed from counting statistics.
[c] n.d. = not determined.

anorthite (Ca*K*α, Al*K*α, Si*K*α), albite (Na*K*α), microcline (K*K*α), fayalite (Fe*K*α), forsterite (Mg*K*α), TiO_2 (Ti*K*α), V_2O_5 (V*K*α), Cr_2O_3 (Cr*K*α), and sodalite (Cl*K*α). Standards for the analysis of hexamolybdenum were the pure metals Mo (*K*α), Fe (*K*α), W (*L*α), Ru (*L*α), Os (*L*α), Ir (*L*α), Ni (*K*α), Pt (*L*α), and Re (*L*α). Quantitative elemental microanalyses were processed with the CITZAF correction procedure (Armstrong 1995) and analytical results are given in Tables 1–2. An Oxford INCA X-ray energy-dispersive spectrometer (EDS) on the ZEISS SEM was also used for elemental analysis. These data were processed using the XPP correction procedure of Pouchou and Pichoir (1991).

The average of eight electron probe microanalyses (EPMA) of allendeite crystals (Table 1) leads to an empirical formula referenced to 12 O atoms of $(Sc_{3.01}Ti^{4+}_{0.44}Ca_{0.31}Al_{0.09}Fe^{2+}_{0.07}Y_{0.04}V^{3+}_{0.03})_{\Sigma 3.99}(Zr_{2.95}Hf_{0.04})_{\Sigma 2.99}O_{12}$. No other elements with atomic number greater than 4 were detected by WDS scans. Given the close adherence to an $X_4Z_3O_{12}$ stoichiometry and the fact that the number of cations of Ti (0.44) in the formula unit is approximately equal to $Ca^{2+} + Fe^{2+}$ (0.40), Ti is dominantly tetravalent, although we cannot exclude the presence of minor amounts of trivalent Ti (<~15% of the total). Assuming that Ti is quadrivalent, allendeite in *ACM-1* can be treated, to first order, as a solid solution $Sc_4Zr_3O_{12}$–$(X^{2+}Ti^{4+})_2Zr_3O_{12}$–$Z^{3+}_4Zr_3O_{12}$, where X refers to divalent cations, Z refers to all trivalent cations other than Sc, and Hf is ignored for simplicity. The $Sc_4Zr_3O_{12}$ component comprises ~85 mol% of allendeite in *ACM-1*.

Figure 4 shows the compositions of allendeite and other Sc-,Zr-enriched phases from carbonaceous chondrites. Allendeite is Sc-enriched relative to tazheranite in *ACM-1* and other zirconias reported in the literature, with the exception of one described by Weber and Bischoff (1994) from a perovskite-rich, grossite-bearing inclusion in the CH chondrite Acfer 182. Based on the close compositional similarity to allendeite, this phase is probably allendeite and not an unusually Sc-rich tazheranite. Panguite and kangite are more titaniferous than allendeite and considerably poorer in Sc and Zr.

Compositions of allendeite, hexamolybdenum, and associated phases in *ACM-1* are given in Tables 1–2. The oxides are highly enriched in Sc. Tazheranite (15 wt% Sc_2O_3) is Sc-rich relative to the meteoritic zirconias reported by other workers [Noonan et al. 1977; Lovering et al. 1979; Hinton et al. 1988; based on composition, we interpret the Sc-,Zr-rich oxide from inclusion 418/P in Acfer 182 described by Weber and Bischoff (1994) as allendeite (i.e., not as tazheranite)]. The included perovskite in *ACM-1* [$(Ca_{0.89}Y_{0.08}Sc_{0.04})_{1.01}(Ti_{0.88}Zr_{0.06}Al_{0.05}Fe_{0.01})_{1.00}O_3$; 2.5 wt% Sc_2O_3] has much less Sc than the tazheranite but it is more Sc-rich than any previous perovskite composition reported in the literature [none to our knowledge exceeding the 1.75 wt% Sc_2O_3 for a perovskite from inclusion 418/P, which also contains Sc-rich oxides (Weber and Bischoff 1994)]. Compositions of the Os-Ir-Mo-W alloy grains indicated by arrows in Figure 2 are, via SEM-EDS: $(Os_{0.65}Ir_{0.14}W_{0.13}Mo_{0.05}Fe_{0.02}Ru_{0.01})$, $(Os_{0.51}Ir_{0.25}W_{0.13}Mo_{0.07}Fe_{0.02}Ru_{0.02})$, and $(Ir_{0.37}Os_{0.35}W_{0.12}Mo_{0.12}Fe_{0.02}Ru_{0.02})$. The first two grains are osmiums assuming the structure, which was not checked, is $P6_3/mmc$, as is observed for all other osmium-rich alloys in this and other refractory inclusions in carbonaceous chondrites (Harries et al. 2012; this study). The third grain is sufficiently Ir-enriched to be an iridium, if it is cubic, or, despite the very low Ru content, a rutheniridosmine if it is hexagonal. The osmiums in *ACM-1* are the most Os- and W-rich meteoritic alloys that we are aware of, aside from grains in a lakargiite ($CaZrO_3$)-bearing inclusion from Acfer 094 (Ma 2011). Alteration phases include sodalite and nepheline. Perovskite in direct contact with alteration phases frequently has thin (<1 μm) rims of ilmenite, which is common on Allende perovskites exposed to alteration products (e.g., Keller and Buseck 1989). The inclusion is partially rimmed by a Al-rich, low-Ti augite.

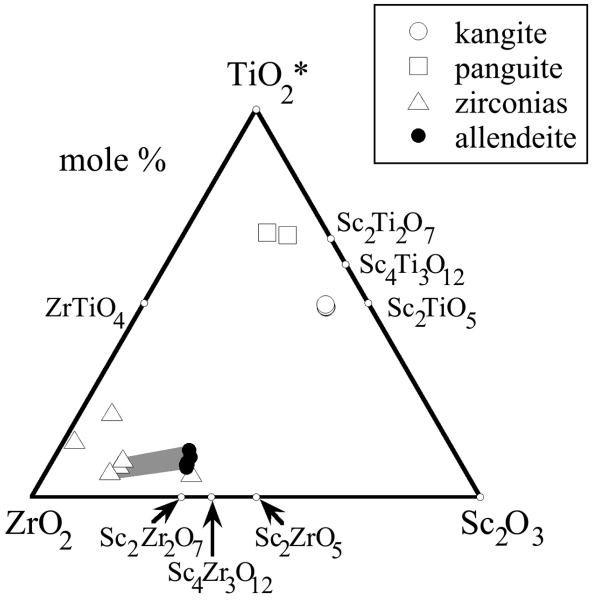

FIGURE 4. Compositions (mol%) of Zr- and Sc-enriched oxides in carbonaceous chondrites in terms of the ternary Sc_2O_3-TiO_2*-ZrO_2, where TiO_2* represents all Ti calculated as TiO_2. Coexisting allendeite and tazheranite from *ACM-1* are connected by a gray tie line. Known synthetic compounds within the system Sc_2O_3-TiO_2-ZrO_2 are plotted as small circles. The "zirconia" that plots near the allendeite from this study is described by Weber and Bischoff (1994). The structure of this phase is not known but, based on composition, it is likely to be an allendeite. Data for meteoritic phases are taken from Noonan et al. (1977), Lovering et al. (1979), Hinton et al. (1988), Weber and Bischoff (1994), Ma and Rossman (2008b), Ma et al. (2012, 2013c), and this study.

CRYSTALLOGRAPHY

Single-crystal electron backscatter diffraction (EBSD) analyses at a sub-micrometer scale were performed using an HKL EBSD system on the ZEISS 1550VP scanning electron microscope operated at 20 kV and 4 nA in a focused beam with a 70° tilted stage in variable pressure mode (20 Pa). The EBSD system was calibrated using a single-crystal silicon standard. The structure was determined and cell constants were obtained by matching the experimental EBSD pattern with known structures of synthetic phases. The HKL software automatically suggests indexing solutions ranked by the lowest "mean angular deviation" (MAD) with MAD numbers below 1 considered desirable for accurate solutions. We used the highest ranked solutions (lowest MAD) for establishing structural matches and obtained MAD numbers of 0.1–0.3 for allendeite, and 0.3–0.4 for hexamolybdenum.

Allendeite

Under most conditions, EBSD cannot be used to determine accurate cell parameters but matches against known structures can be tested very accurately. Electron backscatter diffraction (EBSD) patterns of allendeite determined in the SEM were matched against all of the known structures of synthetic $Sc_4Zr_3O_{12}$ (Thornber et al. 1968; Rossell 1976; Red'ko and Lopato 1991) and the structure of perovskite (Pawar 1967). The EBSD pattern (Fig. 5) was an excellent match to the computed EBSD pattern and cell parameters of synthetic $Sc_4Zr_3O_{12}$ (ICSD collection code 009615, PDF 71-1022) from Rossell (1976), with the MAD numbers as low as 0.12. Alternative structures had much higher MAD values (>0.6). Allendeite is trigonal with space group: $R\bar{3}$, $a = b = 9.363$ Å, $c = 8.720$ Å, $V = 666.7$ Å^3, and $Z = 3$. Note that errors on the cell parameters are not stated because they are taken directly from the data of the matching $Sc_4Zr_3O_{12}$ phase in Rossell (1976). Allendeite has a fluorite-related superstructure. Zirconium and scandium are both seven-coordinated to oxygen, on average, and randomly distributed over two sets of general sites. The calculated density is 4.84 g/cm^3 using the observed chemistry (Table 1) and the cell parameters of Rossell (1976). X-ray powder-diffraction data (in angstroms for Cu$K\alpha_1$) taken from PDF 71-1022 show that the strongest calculated lines are [d in Å, intensity in % relative to that of (12$\bar{1}$), (hkl)]: [2.900 (100) (12$\bar{1}$)], [1.776 (32) (140)], [1.779 (27) (12$\bar{4}$)], [1.515 (19) (143)], [2.513 (18) (21$\bar{2}$)], [4.698 (5) (110)], [1.450 (4) (24$\bar{2}$)], and [1.152 (4) (701)].

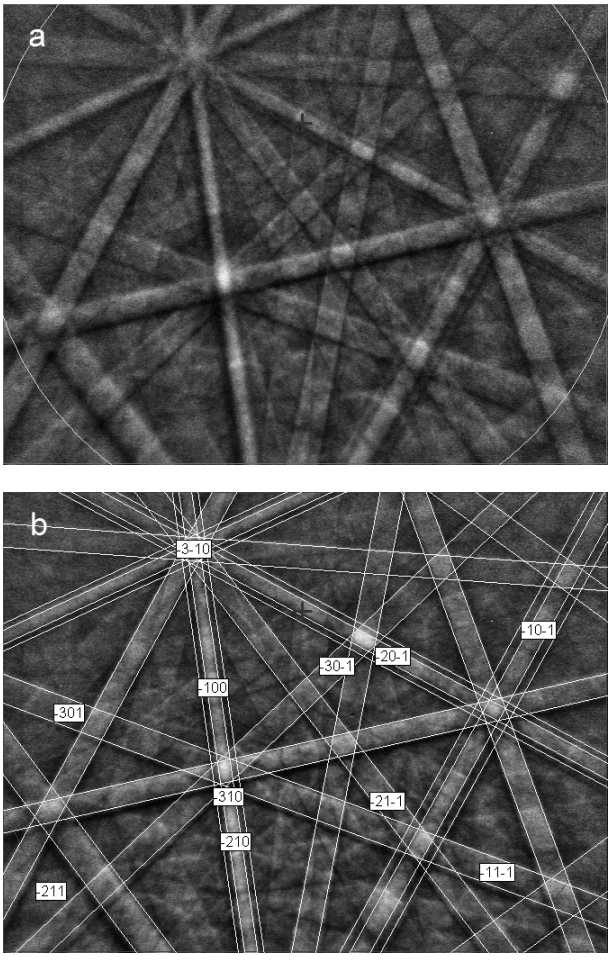

FIGURE 5. (**a**) EBSD pattern of the allendeite crystal shown in Figure 2. The cross indicates the center of the EBSD pattern. Portions of a circle are also shown. This circle encloses the EBSD area used for defining the diffracting bands. (**b**) The EBSD pattern shown in panel (**a**) indexed using the $Sc_4Zr_3O_{12}$ $R\bar{3}$ structure as given by Rossell (1976).

Hexamolybdenum

The hexamolybdenum crystals were too small for conventional single-crystal XRD study, but it was possible to study them using EBSD. The EBSD patterns can be indexed in terms of the $P6_3/mmc$ structure exhibited by Ru (Urashima et al. 1974) and some intermediate Ru-Mo alloys (Anderson and Hume-Rothery 1960; Kraus and Nolze 1996; Park et al. 2000) but not in terms of the cubic $Im\bar{3}m$ structure assumed by Mo (Kleykamp 1988) or tetragonal $P4_2mnm$ Mo-Ru structures (Raub 1954; Anderson and Hume-Rothery 1960; Park et al. 2000). The best fit was achieved using cell parameters of synthetic $Mo_{55}Ru_{45}$ (e.g., Anderson and Hume-Rothery 1960) (Fig. 6), with mean angular deviations as low as 0.27. Hexamolybdenum is hexagonal with space group $P6_3/mmc$, a = 2.7506, c = 4.4318 Å, V = 29.04 Å^3, and Z = 2. It has the same crystal structure as the minerals garutiite (Ni,Fe,Ir), hexaferrum (Fe,Os,Ru,Ir), ruthenium (Ru,Ir,Os), rutheniridosmine (Ir,Os,Ru), and osmium (Os,Ir). The X-ray powder-diffraction data (in Å for Cu$K\alpha_1$) calculated with the empirical formula using the program Powder Cell version 2.4 (e.g., Kraus and Nolze 1996), reveals that the strongest calculated lines are [d in angstroms, intensity in % relative to that of (101), (*hkl*)]: [2.098 (100) (101)], [2.216 (26) (002)], [2.382 (24) (100)], [1.169 (20) (112)], [1.255 (18) (103)], [1.375 (17) (110)], [1.622 (15) (102)], and [1.150 (14) (201)].

In addition to the grains in *ACM-1* described above, we also observed one 650 nm inclusion of hexamolybdenum in perovskite from a fine-grained inclusion in Allende section USNM 3509HC12 (Fig. 7). This crystal has a composition of $(Mo_{0.258}Fe_{0.255}Ru_{0.231}Os_{0.109}Ir_{0.094}Ni_{0.027}W_{0.020}Re_{0.006})$, as shown in Table 2, and an EBSD pattern that can only be indexed with the $P6_3/mmc$ structure. Compositions of the associated phases, perovskite and pyroxene, are given in Table 1. Euhedral hexamolybdenum crystals were also identified as inclusions in krotite and grossite in *Cracked Egg*, a CAI from the NWA 1934 CV3 chondrite [USNM section 7590; see Fig. 3 in Ma et al. (2011)].

Molybdenum-rich alloys have been observed previously by El Goresy et al. (1978) and, more recently, by Berg et al. (2009) and Harries et al. (2012), the latter showing that a compositionally wide spectrum of refractory alloys from Murchison have a $P6_3/mmc$ structure. This is a key characteristic for these minerals. The mineral name for a particular refractory alloy grain in a carbonaceous chondrite then devolves to a name associated with the element present in the highest concentration, even if it constitutes less than 50% of the atoms present. Table 3 shows the current nomenclature for $P6_3/mmc$ alloy minerals. All, except for the Ni-dominant alloy garutiite and Ir-dominant rutheniridosmine, have been reported in meteorites.

Hexamolybdenum has a $P6_3/mmc$ structure that is likely stabilized over the cubic structure of elemental Mo (Kleykamp 1988) by the high concentrations of "contaminant" elements. It is possible that cubic Mo-dominant alloys exist in nature. For example, Bogatikov et al. (2001, 2002) described two irregular micrograins of "native molybdenum" in lunar regolith samples but the structure was not determined and the compositions could only be characterized as pure Mo based on SEM-EDS analyses (highly contaminated by host phases).

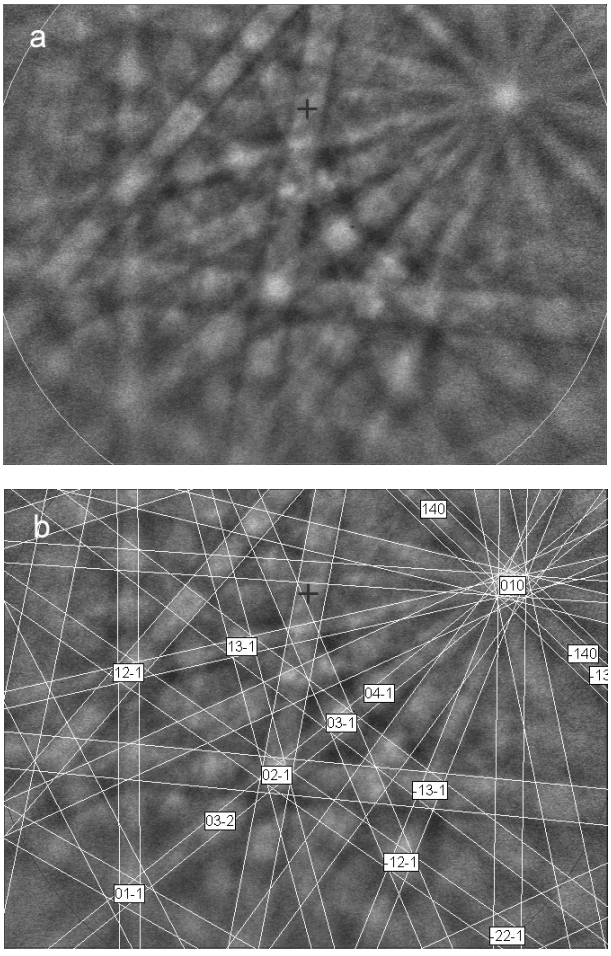

FIGURE 6. (**a**) EBSD pattern of the 1.2 mm hexamolybdenum from *ACM-1* (Fig. 3). The circle and cross have the same meaning as in Figure 5. (**b**) The pattern is best indexed using the $P6_3/mmc$ structure of the synthetic $Mo_{55}Ru_{45}$ phase described by Anderson and Hume-Rothery (1960).

RAMAN SPECTROSCOPY

Raman spectroscopic microanalysis was carried out using a 514.5 nm laser in a Renishaw M1000 micro-Raman spectrometer system on domains of the sample in the polished section previously identified as allendeite crystals through SEM imaging and EBSD analyses. Methods are described in Ma and Rossman (2008a, 2009a). Approximately 5 mW of 514.5 nm laser illumination (at the sample) focused with a 100× objective lens provided satisfactory spectra. The spot size was about 2 μm (i.e., roughly the size of the largest inclusion free portions of crystals). Peak positions were calibrated against a silicon standard. A dual-wedge polarization scrambler was used in the laser beam for all spectra to reduce the effects of polarization.

The Raman spectra of allendeite and the synthetic $Sc_4Zr_3O_{12}$ of Michel et al. (1976) in Figure 8 both show bands in the 700–200 cm^{-1} region but the similarity is not strong. Furthermore, the allendeite spectrum shows strong bands in the 1100–900 cm^{-1} region that are absent in $Sc_4Zr_3O_{12}$. Bands in mineral spectra in

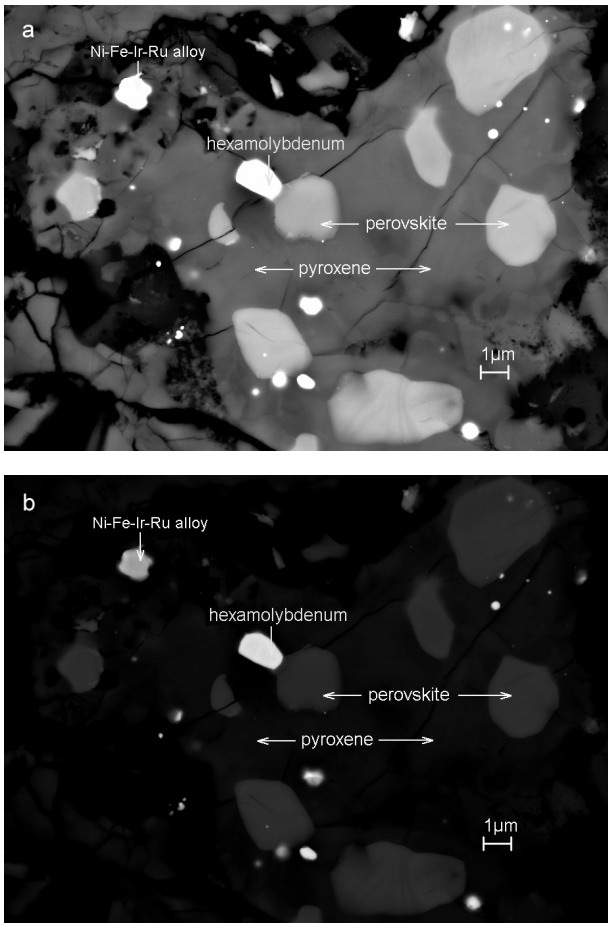

Figure 7. BSE images showing one hexamolybdenum grain in a fine-grained inclusion from USNM polished thin section 3509HC12 with contrast optimized for (**a**) silicates and oxides and (**b**) alloys. Note the difference in Z contrast between hexamolybdenum and the Ni-Fe-Ir-Ru alloy in the upper left of the panel.

this region can reflect laser-induced luminescence of rare-earth elements, a problem encountered with other meteoritic Sc- and Y-enriched phases (e.g., Ma et al. 2013c). We did not detect rare earth elements via EPMA, but laser-induced luminescence can be generated by concentration of the rare earths that are far below the electron microprobe detection limits (Gaft et al. 2005). We conclude that many, and possibly most, of the features of the Raman spectrum of allendeite are caused by rare-earth luminescence rather than arising from intrinsic features of the mineral itself.

Origin and significance

Several minerals with high scandium contents have been found in meteorites including davisite, panguite, kangite, tazheranite, thortveitite, eringaite, and allendeite. Allendeite is the most Sc-rich of these phases (32.4 wt% Sc_2O_3) and only pretulite, $ScPO_4$, a terrestrial phosphate with 49.3 wt% Sc_2O_3, has a substantially more Sc. Hexamolybdenum is part of a continuum of meteoritic refractory alloys with the $P6_3/mmc$ structure that is summarized in Table 3. The mineral names are more obviously descriptive than genetic, but there is value in the

Table 3. Mineral names for $P6_3/mmc$ meteoritic alloys

Dominant element	Mineral name	Example	Reference
Os	Osmium	$Os_{0.35}Ir_{0.21}Mo_{0.26}W_{0.09}Ru_{0.08}$ $Fe_{0.05}Re_{0.02}$	This study
Ir	Rutheniridosmine[a]	–	–
Ru	Ruthenium	$Ru_{0.38}Mo_{0.26}Fe_{0.26}Ni_{0.05}Pt_{0.03}Ir_{0.03}Os_{0.01}$	Harries et al. (2012)
Mo	Hexamolybdenum	$Mo_{0.56}Ru_{0.24}Fe_{0.08}Ir_{0.07}Os_{0.03}W_{0.01}Ni_{0.01}$	This study
Fe	Hexaferrum	$Fe_{0.55}Os_{0.15}Ir_{0.13}Mo_{0.08}W_{0.04}Ru_{0.02}Ni_{0.03}$	Ma (2012)
Ni	Garutiite[a]	–	–

[a] The existence of meteoritic garutiite and rutheniridosmine has not been confirmed. Ni- and Ir-dominant alloys with concentrations of PGEs possibly sufficient to stabilize a $P6_3/mmc$ structure have been reported (e.g., Paque 1989; this study) but the structures of these grains have not been studied.

nomenclature because the names reflect differences in chemistry that connect to the history of the mineral and, therefore, to the history of the host inclusion. In this section, we consider the origin and evolution of *ACM-1* through its constituent phases, particularly of allendeite and hexamolybdenum.

An initial clue to the formation of *ACM-1* lies in the compositions of the constituent phases and the bulk composition of the inclusion. From Figure 1, the inclusion is heavily altered to a mixture of nepheline, sodalite, and augite. Perovskite appears to have survived the alteration event intact, except for some thin ilmenite rims where grains are in contact with alteration phases but allendeite is apparently destroyed as it is observed only where partially protected by perovskite. It is possible that other pre-alteration phases comprised the bulk of what is now alteration products but we see no traces of them, whereas residual allendeite is common within the altered region interstitial to perovskite.

To construct a mode for the precursor inclusion prior to alteration, we begin with perovskite because it is the primary phase least affected by the alteration process. Ignoring possible increases in the volume of the inclusion due to alteration, a point count from Figure 1 yields 24 vol% perovskite. Tazheranite is observed only in the large allendeite grain shown in Figure 1. If this is representative of the inclusion as a whole, prior to alteration, then there was ~ 2 vol% tazheranite. Refractory alloy grains can survive the Allende alteration process(es), although compositions are affected (Paque et al. 2008). However, we

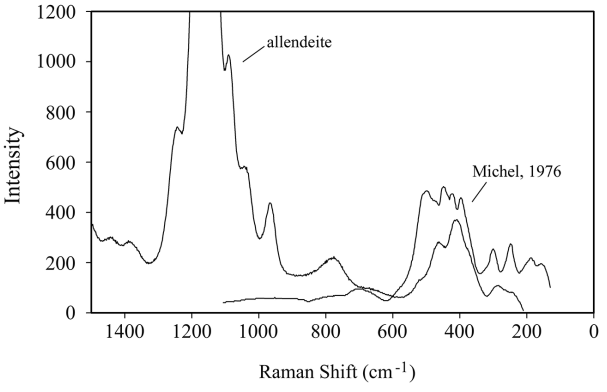

Figure 8. Raman spectrum of allendeite (this study), which has intense bands in the 1300–1000 cm^{-1} region, and synthetic $Sc_4Zr_3O_{12}$ (Michel et al. 1976), which shows no evidence for features in this region of the spectrum.

observed refractory alloys only as inclusions in allendeite or perovskite (i.e., not in the altered regions). We assume that this reflects plucking during section preparation and use the same approach for platinum group element (PGE) enriched alloys that we did for tazheranite, yielding ~1% by volume for the inclusion. If the balance of the inclusion was originally allendeite, then the pre-alteration mode of *ACM-1* was 73% allendeite, 24% perovskite, 2% tazheranite, and 1% alloy (i.e., neglecting the trace spinel). Given average compositions for the phases in *ACM-1* (Tables 1–2) and the densities for allendeite and hexamolybdenum (this study), perovskite (Robie et al. 1979), and tazheranite (Konev et al. 1969; see summary in English in Fleischer 1970), bulk enrichments relative to CI chondrites are 0.5 (Al with spinel neglected), 7 (Ca), 7000 (Y), 30 000 (Sc), 80 000 (Hf), and 90 000 (Zr) for the refractory lithophile elements and 9000–19 000 for Mo, W, Ir, and Os. For individual Mo-Os-W grains, enrichments relative to CI abundances reach 10^5. Although we have not explored REE abundances in the primary minerals, it seems fair to say that *ACM-1* is an ultrarefractory inclusion.

Allendeite and tazheranite

It has long been known that Zr-oxides are extremely refractory in nebular environments as ZrO_2 is the highest temperature oxide to appear in condensation calculations for a cooling gas of solar composition (Grossman 1973; Lodders 2003). Condensation calculations imply that Sc, although quite refractory, is volatile relative to ZrO_2 (Grossman 1973; Kornacki and Fegley 1986; Lodders 2003) with Grossman (1973) calculating the initial condensation of Sc_2O_3, which is not observed in meteorites, Kornacki and Fegley (1986) assuming that Sc condensed in an ideal molecular solution of Sc_2O_3 in $CaTiO_3$ perovskite (meteoritic perovskites can have wt% level concentrations of Sc_2O_3; e.g., Table 1) and Lodders (2003) assigning Sc to hibonite, which condenses at higher temperatures than perovskite. The highly refractory ZrO_2 has a higher condensation temperature than other refractory oxides and undoubtedly accommodates some Sc, but the CI ratio for Sc_2O_3/ZrO_2 is 3.4 by weight, so that, even if condensate tazheranites were all as Sc-rich as the zirconia in *ACM-1* (Table 1), which is unusually scandian, only a small fraction of the Sc in a cooling gas of solar composition could be accounted for through solid solution in zirconia. A similar consideration holds for allendeite ($Sc_2O_3/ZrO_2 \sim 0.6$).

There are various rare Sc-enriched phases in carbonaceous chondrites but most Sc is probably sequestered as a minor to trace element in more common phases. For example, meteoritic hibonites have variable but small concentrations of Sc [18–1316 ppm by weight with an average of 277 ppm for data of Hinton et al. (1988), Ireland et al. (1988, 1991), Sahijpal et al. (2003), and Simon et al. (2002)], but these are in the general range needed to account for a solar Sc/Al ratio (~600 ppm Sc). It is likely that hibonite is a significant sink for Sc in nebular settings. Sc-,Zr-enriched pyroxenes including davisite are not considered in condensation calculations because the thermodynamic properties have not been studied. Also, it is worth noting that, although some Sc-,Zr-enriched oxides may have originated as condensates, crystallization needs to be considered for those occurring in igneous types A and B CAIs (Simon et al. 1991; El Goresy et al. 2002).

Tazheranite can potentially be used as a sensitive indicator of environment through vapor – solid reactions of the type $2ScO_{(g)} + \frac{1}{2}O_{2(g)} = Sc_2O_{3(Taz)}$, where "Taz" refers to tazheranite and "g" to the vapor phase, and solid – solid reactions such as $CaO_{(Taz)} + TiO_{2(Taz)} = CaTiO_{3(Pv)}$, where Pv refers to perovskite. Realizing this potential is difficult because meteoritic tazheranites are compositionally complex (e.g., Table 1). Even neglecting Fe as a possible alteration component, there are wt% level concentrations of Ca, Zr, Hf, Y, and Ti, the latter possibly multivalent. Thus, tazheranite is attractive in providing multiple statements of equilibrium relevant to environments for which we have very little information but it is difficult to quantify these statements because the underlying thermodynamic properties are not sufficiently well constrained.

Even for binary Sc-Zr oxides, there are few data constraining the thermodynamic properties. Jacobson et al. (2001) assessed the system $ScO_{1.5}$-ZrO_2 based mostly on the phase diagram and analogies with the much better constrained system $YO_{1.5}$-ZrO_2. They treated allendeite as a line compound (i.e., composition fixed as $Sc_4Zr_3O_{12}$) and modeled cubic zirconia as a binary solid solution using a Redlich-Kister formalism. The resulting model yields strongly positive deviations from ideality for Sc in cubic zirconia, in contrast to the strong negative deviations obtained by Belov et al. (1987), and shows only fair agreement with the experimentally determined phase equilibria. For the observed composition of tazheranite from *ACM-1* to be consistent with equilibration with host allendeite, large differences in thermodynamic properties relative to those inferred from the model of Jacobson et al. (2001) would seem to be required. For example, the model of Jacobson et al. (2001) could be correct for $ScO_{1.5}$-ZrO_2 but the solution of Ti leads to sharply negative deviations from ideality of the $Sc_4Zr_3O_{12}$ component in allendeite (activity coefficients of ~1/3 or less would be needed). Alternatively, activity coefficients of $ScO_{1.5}$ in tazheranite could be even higher, by 50% or more, than those predicted by Jacobson et al.'s model or the free energy of formation of $Sc_4Zr_3O_{12}$ could substantially more negative than predicted by Jacobson et al. (by 16–21 kJ/mol for temperatures in the range of 800–1500 °C, if cubic zirconia terms were retained). Since the thermodynamic assessment of Jacobson et al. simultaneously fits the thermodynamic properties of all phases in the system, we cannot arbitrarily accept the model parameters for one phase without accepting them for all. We have, therefore, not calculated the stability of $Sc_4Zr_3O_{12}$ allendeite in nebular settings based on the thermodynamic assessment of Jacobson et al. (2001). Additional constraints on the thermodynamic properties of allendeite and Sc-bearing cubic zirconia are needed.

Allendeite is quite rare in carbonaceous chondrites as our continued surveys of Sc- and Zr-enriched phases in Allende and other carbonaceous chondrites have yet to yield another example. The literature contains only one occurrence, described by Weber and Bischoff (1994), which we infer to be allendeite based on the composition. Davisite is, by far, the most common Sc-enriched phase in carbonaceous chondrites. This suggests that allendeite is either the product of a very rare environment or it forms frequently but is readily destroyed through gas-phase reactions. Davisite is a possible endproduct of allendeite altera-

tion and, indeed, of the high-temperature nebular alteration of any Sc-rich oxide but appealing to this phase would require an additional sink for Zr as molar Sc ~ Zr in allendeite but Sc >> Zr in davisite. Certainly, based on *ACM-1*, allendeite is unstable during the alkali-iron metasomatism that altered *ACM-1* and other refractory inclusions in Allende such that there was a net loss of Sc and Zr to the inclusion as there are no Sc-rich phases within or around altered portions of *ACM-1*.

In addition to vapor – solid reactions, allendeite may also be destroyed through dissolution into silicate melts. Based on the phase diagram for Sc_2O_3-ZrO_2, end-member $Sc_4Zr_3O_{12}$ allendeite is extremely refractory. It is stable to ~2100 °C, where it breaks down to form a Sc-rich cubic zirconia of the same composition (Jacobson et al. 2001). Although the upper thermal stability limit for Ti-rich allendeites may be lower than for $Sc_4Zr_3O_{12}$, it seems likely that meteoritic allendeite is thermally stable at peak temperatures for CAI melting (~1400–1500 °C; Stolper and Paque 1986; Richter et al. 2006). If so, the phase would dissolve into the melt, whether congruently (dissolving allendeite-melt interface) or incongruently [intermediate phase(s) produced between allendeite and melt] being indeterminate at present. Allendeite would not simply melt with diffusive homogenization between CAI host melt and an allendeite composition liquid.

If originally present in the precursor phase assemblage of an igneous CAI, allendeite likely dissolves during melting, with the Sc, so released being mostly incorporated into later-crystallizing pyroxene. The relatively common Zr-,Sc-enriched pyroxenes in type A CAIs and in the mantles of type B1s (Simon et al. 1991; El Goresy et al. 2002) could reflect a precursor Zr-Sc oxide that dissolved into the melt with some of the Zr and Sc being subsequently incorporated into crystallizing pyroxene. If so, the Sc_2O_3/ZrO_2 ratio of such a pyroxene would depend on (1) Sc_2O_3/ZrO_2 in the dissolving phase assemblage (~0.6 by weight if only allendeite; lower if perovskite or tazheranite are significant contributors and higher if kangite or panguite are present); (2) how much diffusion occurred in the liquid prior to crystallization of the pyroxene (Sc^{3+} likely diffuses more quickly than Zr^{4+}, so increased dissolution time favors lower Sc/Zr in phases crystallizing in the immediate vicinity of the original Sc-,Zr-enriched phase assemblage); and (3) the ratio of the pyroxene/liquid partition coefficients for Sc and Zr. Taking the effective pyroxene-liquid partition coefficients for Zr (1.1) and Sc (2.8) derived by Simon et al. (1991) for core pyroxenes in type B1 inclusions as approximately correct for Sc-,Zr-rich clinopyroxenes in the mantle, leads to Sc_2O_3/ZrO_2 in initially crystallizing clinopyroxene derived from dissolved allendeite of ~1.3 if no significant diffusion of Sc relative to Zr occurred in the liquid, in reasonable agreement with observed Sc_2O_3/ZrO_2 values (0.8–4.7; average 2.1) in pyroxenes associated with Zr-,Sc-rich perovskite in compact type A inclusions (Simon et al. 1999; El Goresy et al. 2002). Since allendeite has a low Y_2O_3/Sc_2O_3 (0.02), we would also expect low Y_2O_3/Sc_2O_3 in the crystallizing pyroxene, also as observed (0.003–0.013 for data of El Goresy et al. 2002). Thus, allendeite is a plausible candidate for being part of a precursor phase assemblage whose destruction led to the crystallization of Sc-enriched pyroxenes in compact type A inclusions and in the mantles of type B1s.

Hexamolybdenum

A wide variety of refractory metal alloys are observed in Fremdlinge or opaque assemblages of CAIs (El Goresy et al. 1978; Blum et al. 1989) but these probably formed through oxidation/sulfidation at low temperatures of Fe-Ni-rich alloys, possibly leading to exsolution of the observed refractory alloys (Blum et al. 1989). Isolated refractory metal nuggets such as those in *ACM-1* are not the exsolution features of these ferrous alloys. Concentrations of Fe, Ni, and the more volatile of the refractory siderophiles, Pt, Rh, and V in hexamolybdenum and other alloys shown in Figures 1–3 and 7 are quite low (Table 2), as they are in the host phases. These alloys may be relatively pristine examples of early high-temperature condensates or extreme volatilization residues. The euhedral/subhedral habits of hexamolybdenum in *ACM-1* and anhedral habits of those alloys most enriched in Os-Ir-W may reflect a thermal event that attacked the existing alloy grains prior to the condensation of most Mo and Ru (i.e., before the formation of hexamolybdenum).

If volatility is the principal driving force behind the composition of a meteoritic refractory alloys, as suggested by Berg et al. (2009) and Harries et al. (2012), among many others, then the natural composition variables are (Os+W+Re), (Ir), (Mo+Ru), and (Pt+Rh) because these clusters of elements form a series in order of increasing volatility based on their condensation behavior (Campbell et al. 2001). In Figure 9a, elements of intermediate volatility, Ir, Ru, and Mo, are merged and alloy compositions from this study and the literature are plotted in terms of the ternary (Os+W+Re)-(Ir+Mo+Ru)-(Pt+Rh). Alloys from *ACM-1* are restricted to one join because they are very low in Pt and Rh, implying that they are relatively refractory alloys. We expand this join in Figure 9b, where Ir and Ru+Mo, the elements of intermediate volatility, have been separated while still combining the most refractory metals, Os + W + Re. To zeroth order, the data can be described in terms of two lines; one extending from the Os+W+Re (i.e., most highly refractory) vertex toward a second line defined by alloys with chondritic Ir/(Os+W+Re) ratios. From a condensation perspective, such alloys would have Ir, Os, W, and Re fully condensed so that the solution of additional elements leads to the dilution of more refractory elements but not to a change in their ratios). Many alloy compositions are depleted in Ir in this projection and this may reflect subtleties in the thermochemistry, the loss of an iridium-enriched phase in some environments, or, perhaps, systematic analytical errors. Data from this study encompass a broad range of these most refractory compositions [only the alloys analyzed by Ma (2011) appear to have accessed a more refractory set of compositions].

Although the overall trends shown in Figure 9 are consistent with the conclusions of Berg et al. (2009) and Harries et al. (2012) that the alloys represent condensates, there are complications inherent in the data that hint at complexities in process. For example, Figure 10 shows molar Ru/Mo as a function of % Ru + Mo relative to all highly refractory siderophiles, defined for present purposes as Ru+Mo+Ir+Os+W+Re. Most of the data lie near a line extending from low concentrations of Ru + Mo (more refractory), with low Ru/Mo, to higher concentrations of Ru + Mo (less refractory), with Ru/Mo roughly equal to the CI chondrite ratio. There are, however, six compositions that plot at higher Ru/Mo than expected based on the general trend followed by most of

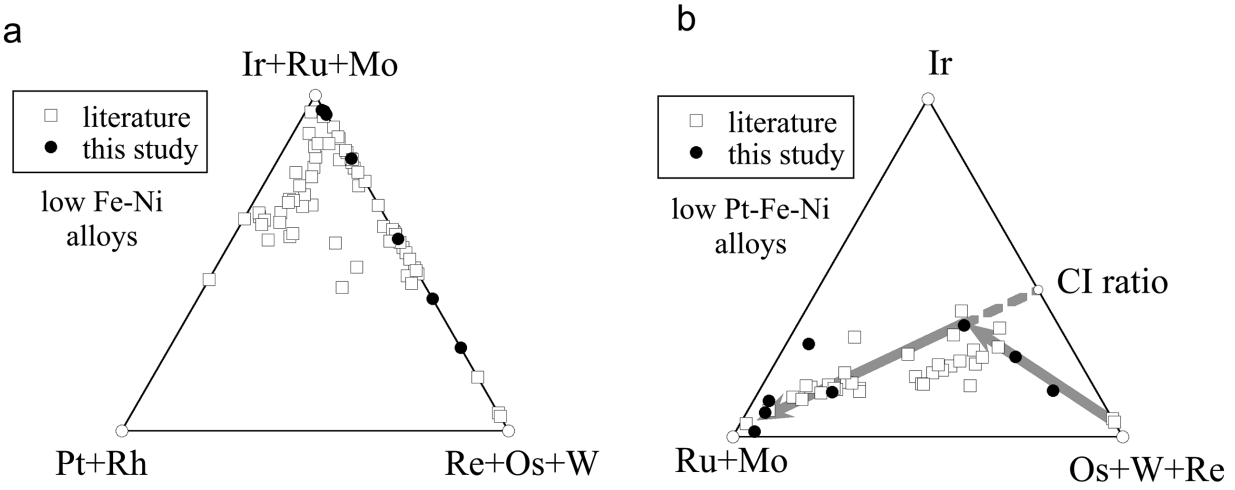

FIGURE 9. Refractory alloy compositions in chondrites (molar basis). Alloys high in the more volatile elements Fe, Ni, and V (sum of mole fractions >0.4) were excluded. Data were taken from Wark and Lovering (1976), Blander et al. (1980), Wark (1986), Lin et al. (1999), Berg et al. (2009), Harries et al. (2012), Croat et al. (2012), Ma (2011), and this study. (**a**) The ternary (Re+Os+W)-(Ir+Ru+Mo)-(Pt+Rh). Alloys from this study have low concentrations of the moderately volatile PGEs Pt and Rh. (**b**) (Re+Os+W)-(Ir)-(Ru+Mo). Gray lines indicate direction of increasing volatility (lower relative temperature of condensation).

the alloys, although none are from *ACM-1*. A simple explanation for these anomalous grains is that they experienced an evaporative event under oxidizing conditions. Fegley and Palme (1985) noted long ago that Mo (and W) are volatile in gases that are oxidizing relative to a gas of solar composition due to stabilization of Mo and W oxides in the vapor. Thus, in Figure 10, the anomalous alloys may have undergone an evaporative (or condensation) event in a gas that was oxidizing relative to a gas of solar composition. Large depletions (60–90% of expected Mo) are implied. Tungsten concentrations were reported in three of these grains, MUR1 and MUR2 from Croat et al. (2012), and a grain in Allende inclusion 3643 described by Wark (1986)]. All three exhibit W depletions. It is perhaps notable that two of the three, MUR1 and MUR2, are included in graphite, which would generally be regarded as an indicator of reducing conditions, and that these are known to be presolar grains (Croat et al. 2012). Molybdenum and W anomalies can also reflect low temperature mobility (e.g., Campbell et al. 2001). If, however, we assume that graphite would have been attacked in an event oxidizing enough to generate the observed Mo and W depletions in MUR1 and MUR2, this suggests that the presolar alloys described by Croat et al. (2012) formed in or were exposed to an oxidizing environment prior to their incorporation in presolar graphite.

Notwithstanding the anomalous grains of Figure 10, most refractory metal grains form a coherent trend in composition, suggesting a common evolution. In the following discussion, we first consider the structures of refractory metal alloys in meteorites. This is important because two phases with identical composition but different structure will have different stabilities as neither the lattice stability nor the solution properties will be the same. We then evaluate the relevant thermodynamic properties and these data are used to calculate alloy compositions for condensation in a cooling gas of solar composition. Through these calculations, we illustrate how hexamolybdenum fits into the broader context of refractory metal alloys in carbonaceous chondrites.

Based on INAA analyses of alloy-rich samples, Sylvester et al. (1993) inferred that early condensation of refractory elements involved at least three different carriers. They noted that end-member platinum group elements (PGEs) and Fe-Ni assumed various structural forms and made the testable prediction that the end-members apparent in their data reflected condensation of refractory alloys into phases with three distinct structures. Harries et al. (2012) showed, however, that the PGE-rich alloys in Murchison invariably have a $P6_3/mmc$ structure [our studies of refractory metal nuggets from Allende and various other carbonaceous chondrites (Acfer 094, Murchison, NWA 1934, Vigarano) have also yielded only $P6_3/mmc$ structures] and they, therefore, concluded that Sylvester et al.'s observed groupings were not due to condensation of refractory siderophiles into multiple structures.

Berg et al. (2009) calculated alloy compositions as a function of temperature in a cooling gas of solar composition referenced to a total pressure of 10^{-4} bars using procedures and thermodynamic data outlined by Campbell et al. (2001) and oxygen fugacities from Rubin et al. (1988). They then obtained an apparent condensation temperature for an analyzed alloy by finding the one that minimized deviations between calculated and observed alloy compositions. There are two key assumptions in the calculations of Berg et al. (2009): (1) Nonideality in the alloy solution can be neglected and (2) lattice stabilization energies for elements in hexagonal structures are the same as for the corresponding elements in their stable structural state. We briefly consider the effects of these assumptions on calculated alloy compositions.

The first assumption is difficult to evaluate in any detail. There are relatively few thermodynamic assessments of binary or higher order systems involving the most refractory elements for Os-Re-Ru-Mo-W-Ir-Pt-Rh alloys. Assessments for Mo-Rh-Ru-Pd-Tc alloys (Kaye et al. 2007) and Mo-W (Gustafson 1988) suggest that activity coefficients, γ_i, in binaries where one element in its pure form has a $P6_3/mmc$ structure (Ru, Tc) with Mo, which has a body center cubic structure, are higher (i.e., more positive) than those

involving binary solid solutions of two cubic or two hexagonal structured end-members. For condensates, a higher activity coefficient for an element *i* in an alloy translates into a lower mole fraction, X_i, because the activity of the element in the condensate, $a_i = \gamma_i X_i$, where γ_i refers to the activity coefficient of element *i*, is dictated by the vapor pressure of that element in the nebula. Thus, a higher value of γ_i in the alloy translates into a lower value of X_i in a condensate alloy and, conversely, a lower value of γ_i results in a higher than expected value of X_i. Qualitatively, Mo and W will be stabilized in the vapor relative to the alloy by this effect relative to other elements in the alloy. Since we cannot explicitly evaluate γ_i in most of the relevant subsystems for $P6_3/mmc$ alloys, we ignore these effects and use an ideal solution model, following Fegley and Palme (1985) and Berg et al. (2009).

The second assumption, that the vapor pressure over hexagonal structured metallic elements is negligibly different from that over the same metal in its stable structural form, can be evaluated quantitatively using available data. Hultgren et al. (1973) tabulated vapor pressures over siderophile elements in their stable structural state as a function of temperature and Campbell et al. (2001) fitted these data to equations of the form

$$\log P_i = -A / T(K) + B \quad (1)$$

for interpolation purposes. In Equation 1, A and B are empirical coefficients, P_i refers to the vapor pressure of element *i* over the pure metal, and *T* is temperature in degrees K.

For the refractory elements with stable hexagonal structures at low pressure (Os, Re, or Ru), the expressions of Campbell et al. (2001) are appropriate standard states for hexagonal structured alloys because the stable pure metals for these elements are also hexagonal. For Mo and W, however, the vapor pressures of Hultgren et al. (1973) refer to values over bcc metals and for Ir, Pt, and Rh, they refer to fcc metals. From the lattice stabilization energies given by Dinsdale (1991), fcc Ir, Pt, and Rh are more stable than the hcp metals by 2–3 kJ/mol. For Mo and W, both of which have stable bcc structures in the temperature range of interest, the difference is larger, up to 12 kJ/mol for Mo and 15 kJ/mol for W. For temperatures between 1000 and 2000 K, these differences translate into vapor pressures over pure metals that are higher than those given in Hultgren et al. (1973) by 0.1–0.2 log units for Ir, Pt, and Rh; 0.3–0.6 for Mo; and 0.4–0.8 for W, with deviations increasing with decreasing temperature.

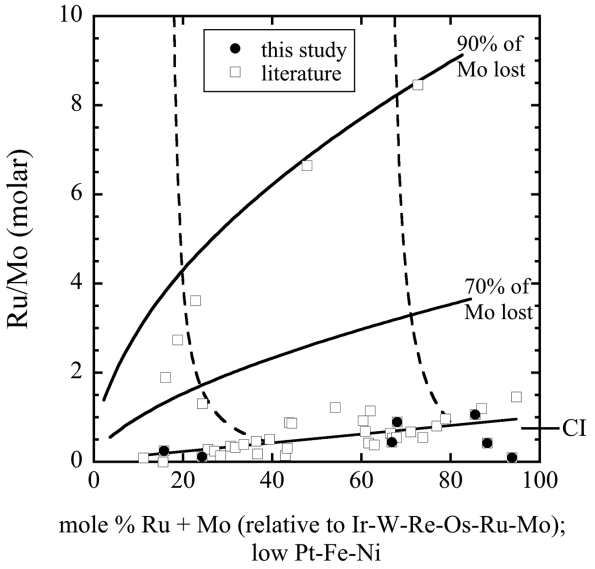

FIGURE 10. Ru + Mo expressed as mol% of the refractory alloy elements that are at least as refractory as Ru and Mo as a function of the molar Ru/Mo ratio. An unweighted regression line is drawn through the data, excluding the six points plotting furthest from the general trend. Dashed curves terminate at the regression line and extend upward through progressive loss of Mo. Solid curves describe the locus of points for specific amounts of the original Mo removed. Data sources as in Figure 9.

We used procedures, oxygen fugacities (via Ebel and Grossman 2000), and thermodynamic data outlined by Campbell et al. (2001) to calculate equilibrium alloy condensate compositions but corrected their expressions for elemental vapor pressures over pure metals to values appropriate for hexagonal metals (Table 4). Campbell et al. (2001) specify activity coefficients for some components in the alloy but we set those to one (i.e., we used an ideal solution). Activity coefficients for these alloys are poorly constrained, as noted above, and, moreover, specifying nonideal activity coefficients for a subset of components, while forcing all others to equal one, would violate the Gibbs-Duhem equation. Our computed alloy compositions show that the effect of lattice stabilization is negligible to modest for total pressures of 10^{-4} bar in the temperature range of greatest interest (~1500–1650 K). Os concentrations can be higher by as much as 0.03 due to destabilization of W, Ir lower by 0.02, and Mo by 0.01. Similar results are obtained if oxygen fugacities of Rubin et al. (1988), which were adopted by Berg et al. (2009), are used.

Hexamolybdenum is part of a continuum of $P6_3/mmc$ alloy compositions but the mineral nevertheless provides a useful genetic context. In Figure 11, we show fields in terms of inverse temperature and total nebular pressure for $P6_3/mmc$ alloy minerals in equilibrium with a cooling gas of solar composition. The plotted lines were calculated assuming an ideal solution for the alloy, using thermodynamic data from Table 4 and Campbell et al. (2001), and employing the calculation procedures of Campbell et al. (2001). Figure 11 may look like a phase diagram but the calculated lines represent conditions for which molar concentrations of the two most abundant elements are equal. This naturally leads to fields within which one element is dominant but, from a thermodynamic perspective, it is important to remember that all of these minerals are the same phase. At any given total pressure, the most refractory meteoritic alloys are osmiums (i.e., Os is the dominant element). With decreasing temperature at a constant

TABLE 4. Parameters for computing the vapor pressure of an element over the crystalline element in a $P6_3/mmc$ structure[a]

Element	A	B
Mo	33201	7.3991
W	44246	7.9608
Ir	34308	7.7100
Pt	29064	7.5936
Rh	28298	7.5415
Co	21393	6.9855
Ni	21447	7.0529
Fe	20532	6.9381
V	26489	7.6338

[a] Elemental Os, Re, and Ru assume stable $P6_3/mmc$ structures, so parameters for these elements are as given in Campbell et al. (2001).

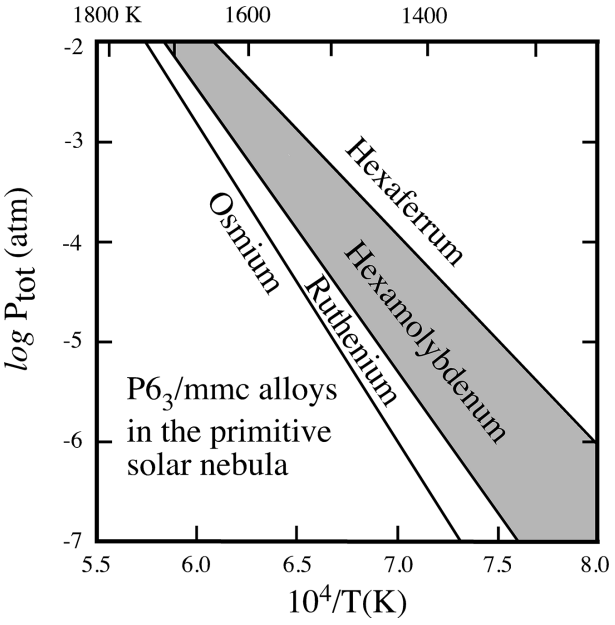

FIGURE 11. Calculated fields for condensate $P6_3/mmc$ mineral alloys in a cooling gas of solar composition. The field for hexamolybdenum is shaded. Lines represent the loci of points for which the two elements with the highest concentrations in the condensate alloy are equal.

pressure, osmium gives way to ruthenium, which is followed by hexamolybdenum and, finally, hexaferrum. In these calculations, Ir is never the dominant element although at least one Ir dominant alloy was observed in *ACM-1* and one might reasonably expect that there is a small field for rutheniridosmine between those of osmium and ruthenium. Stabilization of Ir in the alloy due to nonideality, which is ignored in the calculations, condensation in fractionated nebular gases from which Os has been lost, or kinetic factors may be responsible for the discrepancy. Although not shown, the stability of osmium and hence all $P6_3/mmc$ alloys is limited at high temperatures by vapor (~1840 K at 10^{-4} bar according to Campbell et al. 2001) and at sufficiently high total pressures, by melting. From the perspective of Figure 11, hexamolybdenum is likely "formed" through the incorporation of enough Mo to semantically "destroy" preexisting ruthenium and is itself semantically "destroyed" through the incorporation of enough Fe to make hexaferrum. Hexamolybdenum and other $P6_3/mmc$ alloy minerals may also react with gaseous Fe present in the nebula or a parent body, leading to the formation of a cubic ferrous alloy, the dominant form of Fe-rich alloys in chondrites.

IMPLICATIONS

We describe two new minerals, allendeite and hexamolybdenum, from the *ACM-1* ultrarefractory inclusion from the carbonaceous chondrite Allende and, in so doing, open a new window onto processes during the early stages of the formation of the Solar System. Both phases are likely high temperature condensates. Allendeite ($Sc_3Zr_4O_{12}$) is a potentially important indicator of the evolution of refractory lithophile elements. Hexamolybdenum (Mo,Ru,Fe,Ir,Os) is similarly well posed for evaluating the early distribution of refractory siderophiles.

ACKNOWLEDGMENTS

The Caltech GPS Analytical Facility is supported, in part, by NSF grants EAR-0318518 and DMR-0080065. We also acknowledge NASA grant NNX12AH63G and NSF EAR-0947956. We thank the Smithsonian Institution for additional Allende samples and H.C. Connolly Jr. for bringing them to our attention. The review of A.M. Davis led to significant improvements in the manuscript.

REFERENCES CITED

Anderson, E., and Hume-Rothery, W. (1960) The equilibrium diagram of the system molybdenum-ruthenium. Journal of the Less-Common Metals, 2, 443–450.

Armstrong, J.T. (1995) CITZAF—a package of correction programs for the quantitative electron microbeam X-ray-analysis of thick polished materials, thin-films, and particles. Microbeam Analysis, 4, 177–200.

Belov, A.N., Semenov, G.A., Teterin, G.A., and Shkol'nikova, T.M. (1987) Evaporation and thermodynamic properties of Sc_2O_3 and of ZrO_2-Sc_2O_3 binary solid solutions according to high-temperature mass spectrometry data. II. Calculations. Russian Journal of Physical Chemistry, 61, 468–470.

Berg, T., Maul, J., Schönhense, G., Marosits, E., Hoppe, P., Ott, U., and Palme, H. (2009) Direct evidence for condensation in the early solar system and implications for nebular cooling rates. Astrophysical Journal, 702, L172–L176.

Blander, M., Fuchs, L.H., Horowitz, C., and Land, R. (1980) Primordial refractory metal particles in the Allende meteorite. Geochimica et Cosmochimica Acta, 44, 217–223.

Blum, J.D., Wasserburg, G.J., Hutcheon, I.D., Beckett, J.R., and Stolper, E.M. (1989) Origin of opaque assemblages in C3V meteorites: Implications for nebular and planetary processes. Geochimica et Cosmochimica Acta, 53, 543–556.

Bogatikov, O.A., Gorshkov, A.I., Mokhov, A.V., Ashikhmina, N.A., and Magazina, L.O. (2001) The first finding of native molybdenum, silver sulfide, and iron-tin alloy in the lunar regolith. Geochemistry International, 39, 604–608.

Bogatikov, O.A., Mokhov, A.V., Gorshkov, A.I., Ashikhmina, N.A., Magazina, L.O., Kartashov, P.M., and Koporulina, E.V. (2002) High-quality gold, Cu-Zn-Au-Ag solid solution, and native Mo in the AS Luna 16 regolith. Doklady Earth Sciences, 386, 827–830.

Campbell, A.J., Humayun, M., Meibom, A., Krot, A.N., and Keil, K. (2001) Origin of zoned metal grains in the QUE94411 chondrite. Geochimica et Cosmochimica Acta, 65, 163–180.

Clarke, R.S., Jarosewich, E., Mason, B., Nelen, J., Gómez, M., and Hyde, J.R. (1970) The Allende, Mexico, meteorite shower. Smithsonian Contributions to the Earth Sciences, 5, 1–53.

Croat, T.K., Berg, T., Jadhav, M., and Bernatowicz, T.J. (2012) Presolar refractory metal nuggets. Lunar and Planetary Science Conference, 43, Abstract 1503.

Dinsdale, A.T. (1991) SGTE data for pure elements. CALPHAD, 15, 317–425.

Ebel, D.S., and Grossman, L. (2000) Condensation in dust-enriched systems. Geochimica et Cosmochimica Acta, 64, 339–366.

El Goresy, A., Nagel, K., and Ramdohr, P. (1978) Fremdlinge and their noble relatives. Proceedings of the Lunar and Planetary Science Conference, 9, 1279–1303.

El Goresy, A., Zinner, E., Matsunami, S., Palme, H., Spettel, B., Lin, Y., and Nazarov, M. (2002) Efremovka 101.1: A CAI with ultrarefractory REE patterns and enormous enrichments of Sc, Zr, and Y in fassaite and perovskite. Geochimica et Cosmochimica Acta, 66, 1459–1491.

Fegley, B., and Palme, H. (1985) Evidence for oxidizing conditions in the solar nebula from Mo and W depletions in refractory inclusions in carbonaceous chondrites. Earth and Planetary Science Letters, 72, 311–326.

Fleischer, M. (1970) New mineral names. American Mineralogist, 55, 317–323.

Fuchs, L. (1969) Occurrence of cordierite and aluminous orthoenstatite in the Allende meteorite. American Mineralogist, 54, 1645–1653.

——— (1971) Occurrence of wollastonite, rhönite, and andradite in the Allende meteorite. American Mineralogist, 56, 2053–2068.

Fuchs, L., and Blander, M. (1977) Molybdenite in calcium-aluminum-rich inclusions in the Allende meteorite. Geochimica et Cosmochimica Acta, 41, 1170–1175.

Gaft, M., Reisfeld, R., and Panczer, G. (2005) Modern Luminescence Spectroscopy of Minerals and Materials, Chapter 4. Springer-Verlag, Berlin.

Grossman, L. (1973) Refractory trace elements in Ca-Al-rich inclusions in the Allende meteorite. Geochimica et Cosmochimica Acta, 37, 1119–1140.

Gustafson, P. (1988) An experimental study and a thermodynamic evaluation of the Fe-Mo-W system. Zeitschrift für Metallkunde, 79, 388–396.

Harries, D., Berg, T., Langenhorst, F., and Palme, H. (2012) Structural clues to the origin of refractory metal alloys as condensates of the solar nebula. Meteoritics & Planetary Science, 47, 2148–2159.

Hinton, R.W., Davis, A.M., Scatena-Wachel, D.E., Grossman, L., and Draus, R.J. (1988) A chemical and isotopic study of hibonite-rich refractory inclusions in primitive meteorites. Geochimica et Cosmochimica Acta, 52, 2573–2598.

Hultgren, R., Desai, P.D., Hawkins, D.T., Gleizer, M., Kelley, K.K., and Wagman, D.D. (1973) Selected Values of the Thermodynamic Properties of the Elements. American Society for Metals, Metals Park, Ohio.

Ireland, T.R., Fahey, A.J., and Zinner, E.K. (1988) Trace-element abundances in hibonite from the Murchison carbonaceous chondrite: Constraints on high-temperature processes in the solar nebula. Geochimica et Cosmochimica Acta, 52, 2841–2854.

——— (1991) Hibonite-bearing microspherules: a new type of refractory inclusions

with large isotopic anomalies. Geochimica et Cosmochimica Acta, 55, 367–379.
Jacobson, N.S., Copland, E.H., and Kaufman, L. (2001) Thermodynamic database for the $NdO_{1.5}$-$YO_{1.5}$-$YbO_{1.5}$-$ScO_{1.5}$-ZrO_2 system. NASA Technical Memorandum 2001-210753, 44 pp.
Kaye, M.H., Lewis, B.J., and Thompson, W.T. (2007) Thermodynamic treatment of noble metal fission products in nuclear fuel. Journal of Nuclear Materials, 366, 8–27.
Keil, K., and Fuchs, L.H. (1971) Hibonite [$Ca_2(Al,Ti)_{24}O_{38}$] from the Leoville and Allende chondritic metorites. Earth and Planetary Science Letters, 12, 184–190.
Keller, L.P., and Buseck, P. (1989) Alteration of Ca- and Al-rich inclusions in Allende: A transmission electron microscope study. Lunar and Planetary Science, 20, 512–513.
Kerridge, J.F., and Matthews, M.S. (1988) Meteorites and the Early Solar System, 1269 pp. University of Arizona Press, Tucson.
Kleykamp, H. (1988) The constitution of the Mo-Ru system. Journal of the Less-Common Metals, 136, 271–275.
Konev, A.A., Ushchapovskaya, Z.F., Kashaev, A.A., and Lebedeva, V.S. (1969) Tazheranite, a new calcium-titanium-zirconium mineral. Doklady Academia Nauk SSSR, 186, 917–920 (in Russian).
Kornacki, A.S., and Fegley, B. (1986) The abundance and relative volatility of refractory trace elements in Allende Ca,Al-rich inclusions: implications for chemical and physical processes in the solar nebula. Earth and Planetary Science Letters, 79, 217–234.
Kraus, W., and Nolze, G. (1996) POWDER CELL—a program for the representation and manipulation of crystal structures and calculation of the resulting X-ray powder patterns. Journal of Applied Crystallography, 29, 301–303.
Lauretta, D.S., and McSween, H.Y. (2006) Meteorites and the Early Solar System II, 943 pp. University of Arizona Press, Tucson.
Lin, Y., El Goresy, A., and Ouyang, Z. (1999) Ca-, Al-rich refractory inclusions and Pt-metal nuggets in the Ningqiang carbonaceous chondrite. Chinese Science Bulletin, 44, 725–731.
Lodders, K. (2003) Solar system abundances and condensation temperatures of the elements. Astrophysical Journal, 591, 1220–1247.
Lovering, J.F., Wark, D.A., and Sewell, D.K.B. (1979) Refractory oxide, titanate, niobate and silicate accessory mineralogy of some type B Ca-Al-rich inclusions in the Allende meteorite. Lunar and Planetary Science, 10, 745–746.
Ma, C. (2010) Hibonite-(Fe), $(Fe,Mg)Al_{12}O_{19}$, a new alteration mineral from the Allende meteorite. American Mineralogist, 95, 188–191.
——— (2011) Discovery of meteoritic lakargiite ($CaZrO_3$), a new ultra-refractory mineral from the Acfer 094 carbonaceous chondrite. Meteoritics & Planetary Science, 46 (S1), A144.
——— (2012) Discovery of meteoritic eringaite, $Ca_3(Sc,Y,Ti)_2Si_3O_{12}$, the first solar garnet? Meteoritics & Planetary Science, 47 (S1), A256.
——— (2013a) Majindeite, IMA 2012-079. CNMNC Newsletter No. 15, February 2013, page 10. Mineralogical Magazine, 77, 1–12.
——— (2013b) Nuwaite, IMA 2013-018. CNMNC Newsletter No. 16, August 2013, page 2704. Mineralogical Magazine, 77, 2695–2709.
Ma, C., and Krot, A.N. (2013) Discovery of a new garnet mineral, $Ca_3Ti_2(SiAl_2)O_{12}$: An alteration phase in Allende. Meteoritics & Planetary Science, 48 (S1), Abstract 5049.
Ma, C., and Rossman, G.R. (2008a) Barioperovskite, $BaTiO_3$, a new mineral from the Benitoite Mine, California. American Mineralogist, 93, 154–157.
——— (2008b) Discovery of tazheranite (cubic zirconia) in the Allende meteorite. Geochimica et Cosmochimica Acta, 72, A577.
——— (2009a) Tistarite, Ti_2O_3, a new refractory mineral from the Allende meteorite. American Mineralogist, 94, 841–844.
——— (2009b) Davisite, $CaScAlSiO_6$, a new pyroxene from the Allende meteorite. American Mineralogist, 94, 845–848.
——— (2009c) Grossmanite, $CaTi^{3+}AlSiO_6$, a new pyroxene from the Allende meteorite. American Mineralogist, 94, 1491–1494.
Ma, C., Beckett, J.R., and Rossman, G.R. (2009a) Allendeite and hexamolybdenum: Two new ultra-refractory minerals in Allende and two missing links. Lunar and Planetary Science Conference, 40, Abstract 1402.
Ma, C., Beckett, J.R., Rossman, G.R., Connolly, H.C., Guan, Y., Eiler, J.M., and Hofmann, A.E. (2009b) *In-situ* discovery of a cluster of refractory grains in an Allende ferromagnesian chondrule. Lunar and Planetary Science Conference, 40, Abstract 2138.
Ma, C., Kampf, A.R., Connolly, H.C. Jr., Beckett, J.R., Rossman, G.R., Sweeney Smith, S.A., and Schrader, D.L. (2011) Krotite, $CaAl_2O_4$, a new refractory mineral from the NWA 1934 meteorite. American Mineralogist, 96, 709–715.
Ma, C., Tschauner, O., Beckett, J.R., Rossman, G.R., and Liu, W. (2012) Panguite, $(Ti^{4+},Sc,Al,Mg,Zr,Ca)_{1.8}O_3$, a new ultra-refractory titania mineral from the Allende meteorite: Synchrotron micro-diffraction and EBSD. American Mineralogist, 97, 1219–1225.
Ma, C., Beckett, J.R., Connolly, H.C., and Rossman, G.R. (2013a) Discovery of meteoritic loveringite, $Ca(Ti,Fe,Cr,Mg)_{21}O_{38}$, in an Allende chondrule: Late-stage crystallization in a melt droplet. Lunar and Planetary Science Conferrence, 44, Abstract 1443.
Ma, C., Krot, A.N., and Bizzarro, M. (2013b) Discovery of dmisteinbergite (hexagonal $CaAl_2Si_2O_8$) in the Allende meteorite: A new member of refractory silicates formed in the solar nebula. American Mineralogist, 98, 1368–1371.
Ma, C., Tschauner, O., Beckett, J.R., Rossman, G.R., and Liu, W. (2013c) Kangite, $(Sc,Ti,Al,Zr,Mg,Ca,\square)_2O_3$, a new ultra-refractory scandia mineral from the Allende meteorite: Synchrotron micro-Laue diffraction and electron backscatter diffraction. American Mineralogist, 98, 870–878.
Ma, C., Beckett, J.R., and Rossman, G.R. (2014) Monipite, MoNiP, a new phosphide mineral in a Ca-Al-rich inclusion from the Allende meteorite. American Mineralogist, 99, 198–205.
Michel, D., Perez y Jorba, M., and Collongues, R. (1976) Study by Raman spectroscopy of order-disorder phenomena occurring in some binary oxides with fluorite-related structures. Journal of Raman Spectroscopy, 5, 163–180.
Noonan, A.F., Nelen, J., Fredriksson, K., and Newbury, D. (1977) Zr-Y oxides and high-alkali glass in an amoeboid inclusion from Ornans. Meteoritics, 12, 332–334.
Paque, J.M. (1989) Vanadium-rich refractory platinum metal nuggets from a fluffy Type A inclusion in Allende. Lunar and Planetary Science, 20, 822–823.
Paque J.M., Beckett, J.R., and Burnett, D.S. (2008) Refractory metal nugget as an indicator of alteration processes in a V-rich Ca-Al-rich inclusion. Lunar and Planetary Science, 39, Abstract 1841.
Park, Y.J., Lee, J.-G., Jee, K.Y., Huh, Y.D., and Kim, W.H. (2000) Structural analysis of simulated fission-produced noble metal alloys and their superconductivities. Bulletin of the Korean Chemical Society, 21, 1187–1192.
Pawar, R.R. (1967) Lattice expansion of molybdenum. High Temperatures-High Pressures, 7, 221–226.
Pouchou, J.-L., and Pichoir, F. (1991) Quantitative analysis of homogeneous or stratified microvolumes applying the model "PAP". In K.F.J. Heinrich and D.E. Newbury, Eds., Electron Probe Quantitation, p. 31–75. Plenum Press, New York.
Raub, E. (1954) Die Legierung der Platinmetalle mit Molybdaen. Zeitschrift für Metallkunde, 45, 23–30.
Red'ko, V.P., and Lopato, L.M. (1991) Crystal structure of rare earth zirconates $M_4Zr_3O_{12}$ and hafnates $M_4Hf_3O_{12}$ (M = rare earth). Izvestiya Akademii Nauk SSSR, Neorganicheskie Materialy, 27, 1905–1910 (in Russian).
Richter, F.M., Mendybaev, R.A., and Davis, A.M. (2006) Conditions in the protoplanetary disk as seen by the type B CAIs. Meteoritics & Planetary Science, 41, 83–93.
Robie, R.A., Hemingway, B.S., and Fisher, J.R. (1979) Thermodynamic properties of minerals and related substances at 298.15 K and 1 bar (10^5 Pascals) pressure and at higher temperatures. U.S. Geological Survey Bulletin, 1452, 1–456.
Rossell, H.J. (1976) Crystal structures of some fluorite-related M_7O_{12} compounds. Journal of Solid State Chemistry, 19, 103–111.
Rubin, A.E. (1997) Mineralogy of meteorite groups. Meteoritics & Planetary Science, 32, 231–247.
Rubin, A.E., Fegley, B., and Brett, R. (1988) Oxidation state in chondrites. In J.F. Kerridge and M.S. Matthews, Eds., Meteorites and the Early Solar System, p. 488–511. University of Arizona Press, Tucson.
Sahijpal, S., Marhas, K.K., and Goswami, J.N. (2003) Determination of rare earth and refractory trace element abundances in early solar system objects by ion microprobe. Proceedings of the Indian Academy of Sciences, 112, 485–498.
Simon, S.B., Grossman, L., and Davis, A.M. (1991) Fassaite composition trends during crystallization of Allende Type B refractory inclusion melts. Geochimica et Cosmochimica Acta, 55, 2635–2655.
Simon, S.B., Davis, A.M., and Grossman, L. (1999) Origin of compact type A refractory inclusions from CV3 carbonaceous chondrites. Geochimica et Cosmochimica Acta, 63, 1233–1248.
Simon, S.B., Davis, A.M., Grossman, L., and McKeegan, K.D. (2002) A hibonite-corundum inclusion from Murchison: A first-generation condensate from the solar nebula. Meteoritics & Planetary Science, 37, 533–548.
Stolper, E., and Paque, J.M. (1986) Crystallization sequences of Ca-Al-rich inclusions from Allende: The effects of cooling rate and maximum temperature. Geochimica et Cosmochimica Acta, 50, 1785–1806.
Sylvester, P.J., Simon, S.B., and Grossman, L. (1993) Refractory inclusions from the Leoville, Efremovka, and Vigarano C3V chondrites: Major element differences between Types A and B, and extraordinary refractory siderophile element compositions. Geochimica et Cosmochimica Acta, 57, 3763–3784.
Thornber, M.R., Bevan, D.J.M., and Graham, J. (1968) Mixed oxides of the type MO_2 (fluorite)—M_2O_3. III. Crystal structures of the intermediate phases $Zr_5Sc_2O_{13}$ and $Zr_3Sc_4O_{12}$. Acta Crystallographica, B24, 1183–1190.
Urashima, Y., Wakabayashi, T., Masaki, T., and Teresaki, Y. (1974) Ruthenium, a new mineral from Horokanai, Hokkaido, Japan. Mineralogical Journal, 7, 438–444.
Wark, D.A. (1986) Evidence for successive episodes of condensation at high temperature in a part of the solar nebula. Earth and Planetary Science Letters, 77, 129–148.
Wark, D.A., and Lovering, J.F. (1976) Refractory/platinum metal grains in Allende Calcium-aluminum-rich clasts (CARC's): possible exotic presolar material? Lunar and Planetary Science, 7, 912–914.
Weber, D., and Bischoff, A. (1994) The occurrence of grossite ($CaAl_4O_7$) in chondrites. Geochimica et Cosmochimica Acta, 58, 3855–3877.

MANUSCRIPT RECEIVED JULY 12, 2013
MANUSCRIPT ACCEPTED NOVEMBER 11, 2013
MANUSCRIPT HANDLED BY BEDA HOFMANN